This is the accepted manuscript made available via CHORUS. The article has been published as:

Two-dimensional nitride ordered alloys: A class of ultrawide bandgap semiconductors

Raagya Arora, Ariel R. Barr, Daniel Bennett, Daniel T. Larson, Michele Pizzochero, and Efthimios Kaxiras

Phys. Rev. Materials **8**, L111002 — Published 27 November 2024

DOI: 10.1103/PhysRevMaterials.8.L111002

Two-dimensional nitride ordered alloys: A class of ultra-wide bandgap semiconductors

Raagya Arora,[1,*] Ariel R. Barr,[2,†] Daniel Bennett,[1] Daniel T. Larson,[3] Michele Pizzochero,[4,1] and Efthimios Kaxiras[3,1,‡]

[1] *John A. Paulson School of Engineering and Applied Sciences, Harvard University, Cambridge, Massachusetts 02138, United States*
[2] *Department of Materials Science & Engineering, Massachusetts Institute of Technology, Cambridge, Massachusetts 02139, United States*
[3] *Department of Physics, Harvard University, Cambridge, Massachusetts 02138, United States*
[4] *Department of Physics, University of Bath, Bath BA2 7AY, United Kingdom*

(Dated: November 14, 2024)

Ultra-wide bandgap (UWBG) semiconductors are poised to transform power electronics by surpassing the capabilities of established wide bandgap materials, such as GaN and SiC, owing to their capability to operate at higher voltage, frequency, and temperature ranges. While bulk group-III nitrides and their alloys have been extensively studied in the UWBG realm, their two-dimensional counterparts remain largely unexplored. Here, we examine the stability and electronic properties of monolayers of ordered boron-based group-III nitride alloys with general formula $B_xM_{1-x}N$, where M = Al, Ga. On the basis of *ab initio* calculations we identify a number of energetically and dynamically stable structures. Instrumental to their stability is a previously overlooked out-of-plane displacement (puckering) of atoms, which induces a polar ordering and antiferroelectric ground state. Our findings reveal the energy barrier between metastable ferroelectric states is lowered by successive switching of out-of-plane displacements through an antiferroelectric state.

I. INTRODUCTION

Ultra-wide bandgap (UWBG) semiconductors have recently emerged as a promising class of materials with the potential to advance power electronics, optoelectronics, and radio frequency devices [1]. Defined by a bandgap ϵ_{gap} exceeding that of gallium nitride (GaN, ϵ_{gap} = 3.4 eV), UWBG materials are resistant to electrical breakdown and exhibit high thermal conductivity and mechanical strength, which enable them to handle high voltages and efficiently dissipate heat. For decades, the landscape of UWBG semiconductors employed in power- and optoelectronics has been dominated by established bulk materials. Examples include Ga_2O_3, diamond, MgZnO, indium tin oxide, indium gallium zinc oxide, and group-III nitrides (GaN, AlN, $Al_xGa_{1-x}N$) [1–3].

As Moore's law nears its end, traditional UWBG semiconductors will face challenges to meet the demands of future high-performance (opto)electronic devices. In response, research is shifting towards low-dimensional materials with novel structures and adaptability. Fueled by the discovery of graphene in 2004 [4], the field of 2D materials has experienced exponential growth, yielding promising candidates for 2D UWBG semiconductors that include group-III metal chalcogenides (GaS, GaSe), metal oxyhalides, metal nitrides, and metal oxides [3]. These materials offer unique possibilities for design and fabrication of next generation high-power transparent electronic devices, deep-ultra-violet photodetectors, flexible electronic skins, and energy-efficient displays [2, 5].

In the present work we focus on boron-based group-III nitrides in 2D structures, since bulk hexagonal boron nitride (hBN) is one of the most stable known UWBG materials. hBN exhibits high thermal conductivity, high chemical stability, mechanical strength, and high quality single crystal and multilayer growth [6, 7]. Other variants, including hexagonal aluminium nitride (hAlN) and gallium nitride (hGaN), also exist in a planar structure and exhibit exceptional electronic, optical, and thermoelectric properties [8].

The combination of bulk AlN and GaN yields the UWBG alloys $Ga_xAl_{1-x}N$ [9]. Bulk AlN exhibits a significantly wider bandgap (6 eV) than GaN (3.4 eV), so the combination results in tunable bandgaps across a broad energy range for $Ga_xAl_{1-x}N$ alloys. These bulk alloys offer additional advantages including exceptional breakdown fields exceeding 10 $MV{\cdot}cm^{-1}$, and high electron mobility reaching up to 1000 $cm^2{\cdot}V^{-1}{\cdot}s^{-1}$[9]. Further, n-type doping with Si is easily accomplished in bulk $Ga_xAl_{1-x}N$ due to its low donor ionization energy [10].

In the case of B-based group III nitrides, the structural and bonding environment presents significant challenges arising from the inherent differences in the preferred bulk crystal structures of BN and AlN or GaN [11] : BN exhibits a thermodynamically stable hexagonal phase, whereas AlN and GaN adopt a wurtzite structure. This disparity hinders the straightforward incorporation of boron into the wurtzite structures of AlN or GaN. Recent efforts have focused on overcoming this challenge by developing thin films of wurtzite $B_xAl_{1-x}N$ on substrates like AlN and sapphire [12]. Earlier computational studies [13–15] offer a deeper understanding of the structure and

* raagya@g.harvard.edu
† Co-First Author.
‡ kaxiras@g.harvard.edu

bonding environment of bulk wurtzite $B_xAl_{1-x}N$. In this work we explore the stable, two-dimensional ordered alloy phases of hBN, namely $B_xM_{1-x}N$ with M=Al or Ga. The aim of this study involves thorough investigation of ordered alloys, aiming to reveal atomic insights into their electronic properties through a definitive characterization of local features and their quantitative correlation.

II. RESULTS AND DISCUSSION

A. Energetic and dynamic stability

While other 2D hexagonal group-III nitride alloys such as $Ga_xAl_{1-x}N$ and $Ga_xIn_{1-x}N$ have been theoretically proposed, stable 2D B-based nitride alloys have not been demonstrated [16]. Previous works focused on planar geometries and did not thoroughly explore possible thermodynamically and dynamically stable crystal structures. Here we identify a critical factor for the stability of 2D B-nitride alloys, namely out-of-plane distortion (puckering) of the crystal structure, which can impact stability, enhance spin-orbit coupling, and break the sublattice symmetry associated with the isotropic planar structure, thus modifying the electronic, thermal, and topological properties [17, 18]. For example, puckered monolayer 2D Xenes such as silicene exhibit exotic electronic and magnetic properties [19] such as giant magnetoresistance [20], chiral superconductivity [21], and the quantum spin Hall effect [22] which are not exhibited by their planar crystalline counterpart. The highly corrugated structure of 2D black phosphorus similarly results in a novel response to applied stimuli such as strain, electric field, or polarized light, which do not occur in the bulk structure [23–25]. In a similar vein we find that the puckered structures of $B_xM_{1-x}N$ exhibit an unusual antiferroelectric (AFE) ground state, through which polarization switching between metstable ferroelectric (FE) states occurs. This phenomenon gives rise to a three-state system with potential applications in low-dimensional non-volatile memory devices [26]. The competition between FE and AFE ordering within the B-based alloys allows the superstructure to persist even in monolayer crystals.

To gain a detailed understanding of the properties of B-based nitride alloys and motivate their experimental realization, we present an *ab initio* study of their structural and electronic properties using semi-local and hybrid density functional theory (DFT) calculations. We consider the B-based group-III nitrides $B_xM_{1-x}N$ where M = Al, Ga, for x = 0, 0.25, 0.50, 0.75, 1, using 2D hexagonal structures in 2×2 and 4×4 supercells of the primitive cell of hBN. The thermodynamic stability of an alloy is determined by the heat of formation, defined by $\Delta H_f = E_{tot} - \sum_n \mu_n \eta_n$ where E_{tot} is the total energy of the 2D alloy structure, η_n is the concentration of element n in the alloy, and μ_n is the chemical potential of element n, which by convention is taken to be the total energy per atom of the constituent elements (Al, B, N, Ga) in their most stable reference state. The thermodynamic stability of the various alloys we consider is summarized in Table 1. For materials with comparable puckered and planar heat of formation, the soft phonon modes of the planar structure act as a driving force to spontaneously transform to a dynamically stable puckered crystal.

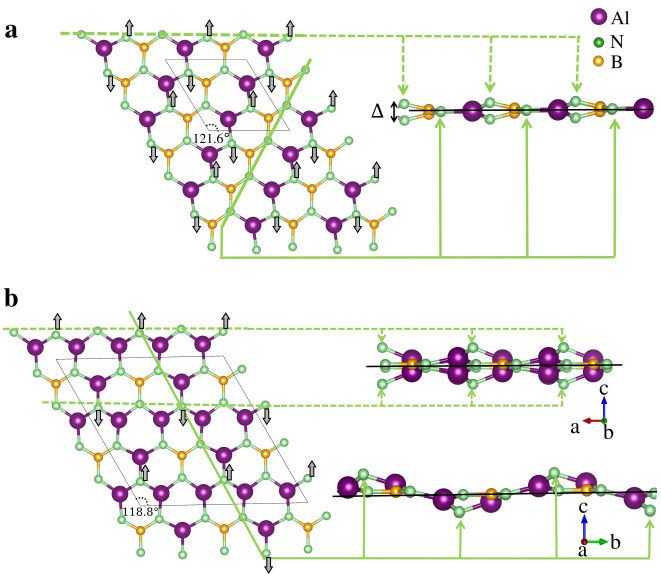


FIG. 1. Top and side views of stable 2D polar hexagonal monolayers of $B_xAl_{1-x}N$ with Al concentration **(a)** x = 0.5, **(b)** x = 0.75. The up and down arrows indicate the out-of-plane displacements (Δ) of N atoms relative to the ideal planar geometry. The 2×2 supercell for x = 0.5 and the 4×4 supercell for x = 0.75 are highlighted in black.

All hexagonal $B_xAl_{1-x}N$ and $B_xGa_{1-x}N$ alloys we consider have negative heat of formation, which is a necessary condition for stability. Among the pure binary hexagonal Al/B/Ga nitrides (point group D_{3h}, space group #194, $P6_3/mmc$), hBN exhibits the lowest per atom ΔH_f, followed by AlN and then GaN. This trend aligns with the known stability of hexagonal phases of these materials, in comparison to the wurzite structures. For a fixed composition x, $B_xAl_{1-x}N$ alloys consistently display lower per atom ΔH_f values compared to $B_xGa_{1-x}N$ alloys.

To assess the dynamical stability of group-III nitride alloys in 2D form, we calculate the phonon spectra using density functional perturbation theory (DFPT). For the pure phases BN, AlN, and GaN, the calculated phonon spectra show no imaginary frequencies (see Fig. S1 in Supplementary Information [54] see also references [55-61] therein), confirming their dynamical stability in the hexagonal planar configuration. Furthermore, these pristine III-V nitride monolayers exhibit insulating behavior in their planar geometries, with indirect band gaps of 5.71 eV, 4.04 eV, and 3.76 eV for BN, AlN, and GaN, respectively, as calculated with the HSE hybrid functional. The prevalence of strong sp^2 bonding in these structures

TABLE I. Evolution of the heat of formation (ΔH_f in eV/atom) and bandgap (ϵ_{gap} in eV) of 2D nitride ordered alloys as a function of boron content (x).

Material	x =	0.00	0.25		0.50		0.75	1.00
		planar	planar	puckered	planar	puckered	planar	planar
$B_xAl_{1-x}N$	E_f	−0.97	−1.25	−1.26	−1.10	−1.11	−1.07	−1.25
	ϵ_{gap}	4.04	4.09	4.20	4.52	4.73	5.16	5.71
$B_xGa_{1-x}N$	E_f	−0.16	−0.23	−0.24	−0.27	−0.30	−0.63	
	ϵ_{gap}	3.76	3.76	4.45	3.96	4.17	5.26	

allows the group-III cations to adopt a planar geometry.

On the other hand, 2D alloys of BN with Al or Ga adopt a puckered structure. Fig. 1 shows two specific examples: $B_{0.5}Al_{0.5}N$ and $B_{0.25}Al_{0.75}N$. The hexagonal planar structure of $B_{0.5}Al_{0.5}N$ has a wide band gap of 4.52 eV. The atom-projected electronic structure is presented in Fig. 2(a) and Fig. S2, and exhibits well separated valence bands composed of Al and B atom s and p orbitals, while the conduction band is composed of N s and p orbitals. The valence band at Γ primarily consists of N atom out-of-plane p_z orbitals while the valence band at the M and K points is composed of in-plane N p_x,p_y orbitals. The interaction between p_z orbitals and p_x,p_y orbitals of anions in the planar lattices vanishes due to the horizontal reflection symmetry. The inset of Fig. 2(a) shows the calculated charge density plot, which confirms the prevalence of sp^2 bonding in these structures that allows the B cations to adopt a trigonal planar geometry. Achieving and maintaining a planar geometry in B-based alloys at different concentrations relies on strong π-bonding between the p_z obitals [27], similar to graphene and hBN.

Fig. 2(c) shows the phonon spectrum of planar $B_{0.5}Al_{0.5}N$. The presence of imaginary frequencies throughout the spectrum (red lines) indicates dynamical instability in this structure. Further analysis of the phonon eigenvectors at Γ confirms that the soft modes correspond to the out-of-plane displacements of the N atoms with either the same or opposite signs in the zigzag and arm chair directions, respectively. These soft modes act as a driving force, spontaneously transforming the planar $B_{0.5}Al_{0.5}N$ structure into a lower-energy stable phase. The dynamical stability of these new puckered phases is confirmed by their phonon spectra, shown in Fig. 2(d) and Fig. S3, which display no imaginary frequencies.

B. Polar ordering and Chemical Bonding

Polar phases in two-dimensional (2D) materials are of importance for advanced semiconductor applications, such as ferroelectric field-effect transistors (FeFETs). In these devices, the polarization of ferroelectric materials can induce charge carriers in adjacent layers. The sense of the doping (electrons or holes), can be changed by inverting the polarization in the ferroelectric material with an electric field. State of the art FeFETs have recently been developed using 2D materials, using ferroelectric rhombohedral (3R) bilayer hBN to dope a neighboring layer [28]. 2D FeFETs have very promising properties in terms of applications, with a polarization that survives at room temperature and can be switched over a large number cycles (10^{11}) without any signs of fatigue. This showcases the innovative potential of leveraging polar phases of 2D materials for novel device architectures.

Polar ordering emerges as a consequence of the N atom distortions along the out-of-plane direction, which stabilize an anti-ferroelectric (AFE) phase of $B_{0.5}Al_{0.5}N$. Consistent with the soft modes observed at Γ in the planar structure, in the puckered structure the N atoms bonded to two Al atoms are displaced in opposite directions, while the remaining two N atoms which are bonded to two B atoms prefer to remain in-plane. The stable puckered structure of $B_{0.5}Al_{0.5}N$ is an hexagonal structure with lower symmetry, with lattice constants a=5.67, b= 5.53 Å and angle $\gamma = 121.6°$ that deviates slightly from 120° (Fig. 1(a)). We carried out a similar analysis of the structures of nitride alloys with gallium instead of Al (see SI for details).

Puckering of the lattice lowers the energy by 7 meV/atom and further opens the bandgap (Fig. 2(b) and Fig. S6 of SI). We present a detailed analysis of the orbital-projected electronic structure of $B_xAl_{1-x}N$, (see Fig. 2 and Fig. S6) at various concentrations. As is clear in Fig. 2(b), the out-of-plane distortion leads to notable changes in the bands with N p_z and p_x, p_y character. Puckering lowers the lattice symmetry and permits previously symmetry-forbidden mixing between p_z and p_x, p_y orbitals, which pushes the N-p_z-derived orbitals to lower energy and increases the bandgap. The origin of puckering at high concentrations of Al/Ga ($x < 0.75$) in hBN alloys can also be understood in terms of the atomic radii of B, Al, and Ga, which are 85, 125, and 130 pm, respectively. Large atomic size differences between Al/Ga and B atoms in their trigonal environment introduce a heterogeneous bonding environment, with the ensuing strain being relieved by the lower energy puckered configuration.

Puckering also affects the character of the chemical bonding [27]. Strong π-bonding between the p_z orbitals

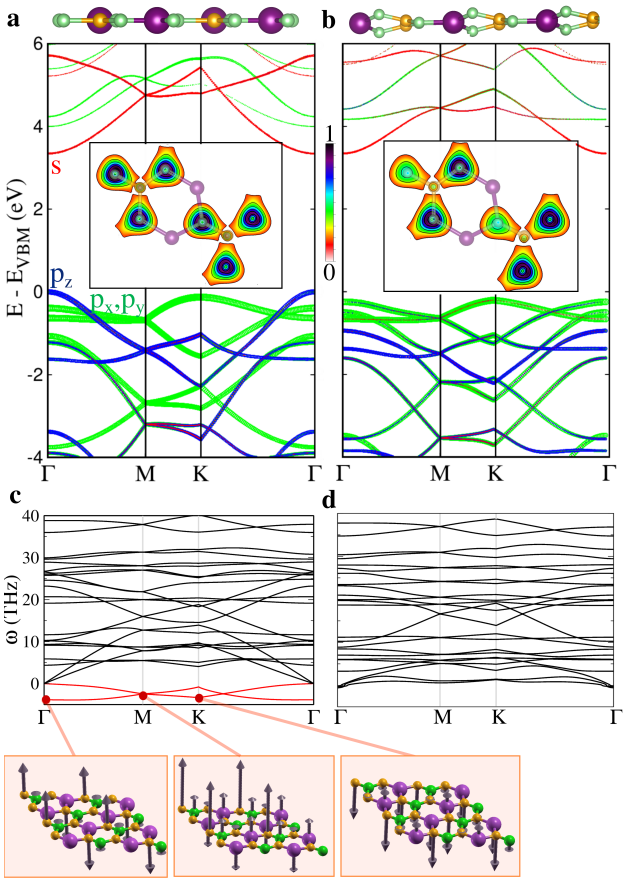


FIG. 2. Electronic structure of $B_{0.5}Al_{0.5}N$ projected onto s and p orbitals of N-atoms: **(a)** hexagonal planar and **(b)** distorted hexagonal puckered structures. **(c)** Phonon dispersion of the planar structure reveals significant instability throughout the Brillouin zone (red lines) absent in the stable puckered structure **(d)**. The three panels below **(c)** show the atomic displacements due to unstable phonon modes at various high-symmetry points indicated by red dots. The insets in (a) and (b) show 2D charge density maps for the planar and puckered $B_{0.5}Al_{0.5}N$.

of B and N atoms is crucial for maintaining a stable planar geometry, but as the concentration of the larger Al atoms increases ($x < 0.75$), the average bond length between nearest neighbors increases. For example, at $x = 0.5$, the average B-N bond length changes from 1.47 Å in the planar geometry to 1.51 Å in the puckered lattice. This increase in bond length weakens the π-bonding due to the decreased overlap of p_z orbitals, and destabilizes the planar geometry in $B_xAl_{1-x}N$ alloys. The inset of Fig. 3(a) shows the isosurfaces of charge density associated with the VBM at Γ for the puckered alloy with $x = 0.25$, demonstrating the weaker overlap between neighbouring p_z orbitals. Thus, puckering disrupts the planar sp^2 hybridization, causing the s, p_x, and p_y orbitals to recombine with the p_z orbital to form orbitals closer to sp^3-like hybridization. The weak interaction between the hybrid orbitals is reflected in the dispersion of the corresponding electronic bands, explaining the occurrence of flat valence bands in the puckered electronic structure of $B_{0.25}Al_{0.75}$ and $B_{0.25}Ga_{0.75}N$ (see Fig. 2b). Alterations in the electronic structure, particularly variations in the valence band maximum (VBM) and conduction band minimum (CBM), have significant implications for a material's ionization energy and electron affinity. These changes critically influence the positioning of dopant levels within the bandgap, determining whether these levels are classified as shallow or deep[29–32]. In turn, this affects the efficiency of doping, as shallow dopant levels typically enhance carrier activation, thereby improving semiconductor performance. Understanding and controlling these electronic structure modifications are crucial for optimizing doping strategies in ultra-wide bandgap semiconductors. This topic is comprehensively addressed in our follow-up work, where we investigate these variations in detail.

The periodic supercell used for structural optimization must be large enough to capture the atomic relaxation in the ground state structure of $B_{0.25}Al_{0.75}N$. While a 2×2 supercell hosts a metastable ferroelectric (FE) state (Fig. S7), a larger 4×4 supercell reveals a lower-energy AFE ground state (Fig. 1(b)), overlooked in earlier studies[5]. The interplay between out-of-plane atomic displacements leads to interesting polar ordering in these alloys, namely a metastable FE state and a stable AFE ground state in $B_{0.25}Al_{0.75}N$. The electronic band structures for both phases are similar, as shown in Fig. 3(a). However, the AFE phase, where N atoms in neighboring cells have an alternating out-of-plane displacements, is approximately a factor of two lower in energy than the FE phase, with respect to the planar paraelectric (PE) phase, see Fig. 3(b) and (c). In the FE phase the inversion symmetry is broken by the out-of-plane displacements of the N atoms, which results in a dipole moment $\vec{p}_z$. The dipole moment as a function of out-of-plane displacement is obtained by calculating the Berry phases[33, 34] from DFT, see Fig. 3(d). The computed energy versus buckling displacement u (see Fig. S7) of $B_{0.25}Al_{0.75}N$ reveals a double-well potential, with the dipole moment given in terms of the equilibrium value in the FE phase, $p_{\mathrm{FE}} = 4.83\times10^{-22}$ C · m. The AFE phase is characterized by an alternating pattern of out-of-plane displacements and has considerably lower energy than the FE phase. A zero total dipole moment is found for every alternating pattern of displacements. In order to distinguish the AFE phase from a PE phase, we calculate the local polarization [35] in each cell using the Born effective charges [36, 37], defined as

$$Z^*_{\kappa,\alpha\beta} = \frac{\partial p_\alpha}{\partial u_{\kappa,\beta}} \tag{1}$$

where $u_{\kappa,\beta}$ is the displacement of atom κ in direction β with respect to the nonpolar configuration. Z^* is approximately constant as a function of displacement, and the

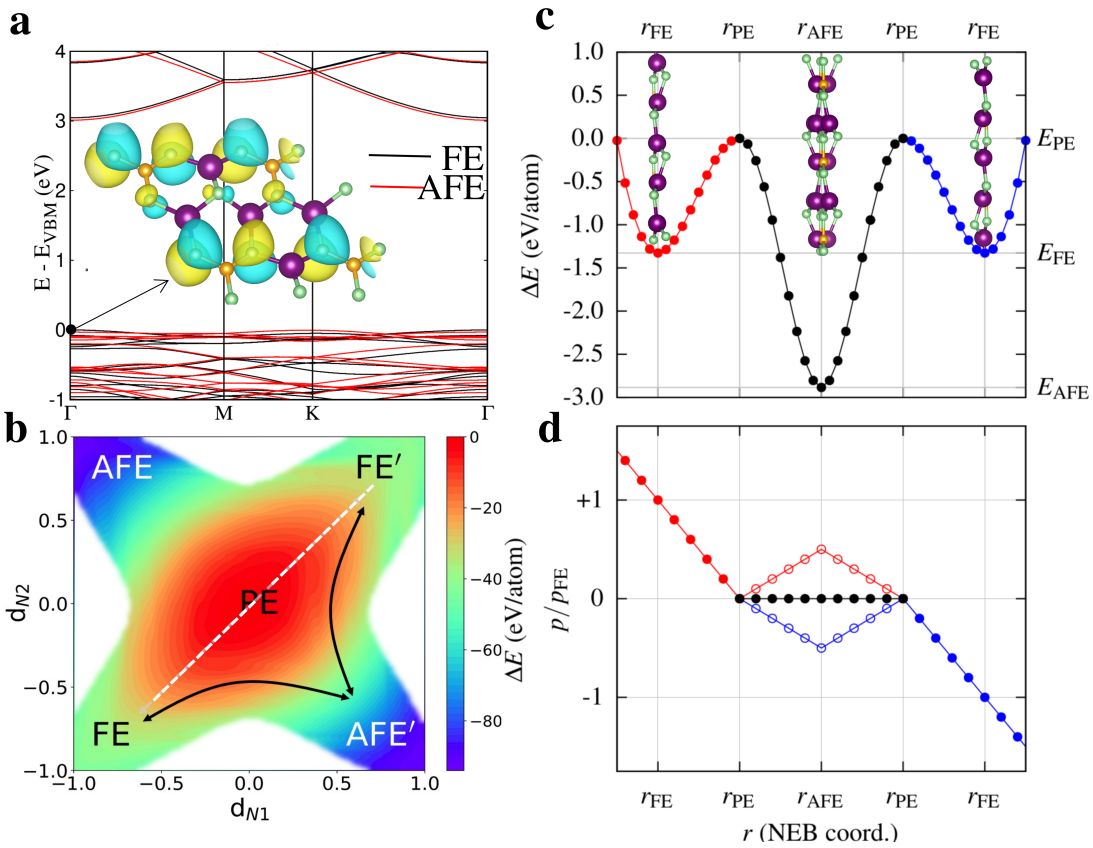


FIG. 3. **(a)** Electronic band structure of $B_{0.25}Al_{0.75}N$ in the FE (black) and AFE (red) phases. The inset shows charge density isosurfaces of the VBM state at Γ for the AFE phase. **(b)** Difference in energy with respect to the PE phase as a function of the out-of-plane displacement of the N atoms in a 2×1 supercell. The displacements d_{N_i}, $i = 1, 2$, are in units of the equilibrium displacement for the FE/AFE phases. The dashed white line indicates the energetically costly switching path through the PE phase, while the solid black arrows denote a lower-energy switching path through an AFE phase. **(c)** Total energy per atom as a function of NEB coordinate r (b). The FE and AFE structures are shown in insets. The FE and AFE phases are separated by the dynamically unstable PE phase. The red and blue points indicate polarization with positive and negative signs, respectively, and the black points indicate zero total polarization. **(d)** Out-of-plane dipole moment as a function of NEB coordinate r, in units of the dipole moment of the FE phase. The filled symbols indicate the total dipole per unit cell, and the open symbols in the AFE region show the local contributions in each cell, which are equal and opposite, verifying that the phase is indeed AFE.

local dipole (Fig. 3 (d)) in each cell i can therefore be calculated as

$$p_z^i = \sum_{\kappa \in i, \beta} Z^*_{\kappa, z\beta} u_{\kappa, \beta}, \tag{2}$$

where the sum over atoms is confined to cell i. In the AFE phase there are nonzero local dipole moments in each cell, which are equal and opposite and half the magnitude of the dipole moment in the FE phase (Fig. 3 (d)).

In FE materials, the direction of the spontaneous polarization can be switched using an external electric field, hence it is important to understand the kinetics of the polarization reversal process. In order to explore the most favorable transition pathway connecting the two energetically degenerate FE states with opposite polarization directions, we systematically scanned the energy surface with respect to two independent reaction coordinates, d_{N_1} and d_{N_2}, which describe the polar displacements of distinct N atoms in the individual cells. Rather than switching polarization through the PE state, the large energy barrier is avoided by passing through the AFE state, as indicated by the black arrows in Fig. 3(b). We used the nudged elastic band (NEB) method to identify the transition pathways and determine the energy barriers between the different ferroelectric states. The energy barrier for switching is sufficiently high to ensure the presence of three distinct states that could be exploited for nonvolatile memory applications: $(+p_z, 0, -p_z)$.

Similar to our findings, the competition between AFE and FE order has been predicted in other 2D materials such as $CuInP_2S_6$[38]. Although a large energy barrier is predicted by DFT, in realistic scenarios the barrier is typically orders of magnitude lower because switching occurs through the nucleation and motion of domain walls. The description of domain walls in these alloys is beyond the scope of this work and is left as a subject of future

research.

III. SUMMARY AND CONCLUSIONS

The integration of 2D materials onto substrates is essential for their practical applications, as substrates can significantly impact their structural and electronic properties. In this study, we focus on the intrinsic properties of puckered hexagonal Group III nitrides, isolated from substrate effects, to establish baseline insights into their stability and electronic characteristics. The example of silicene, which retains its electronic properties when epitaxially grown on substrates like Ag(111), Ir(111) and ZrB_2[39–41], suggest that alloys examined here may similarly maintain their inherent characteristics through weak van der Waals interactions with suitable substrates such as SiO_2 or h-BN. Although detailed studies on substrate interactions are beyond the current research scope, they are an important aspect requiring further exploration.

In conclusion, our first-principles investigation into ordered two-dimensional hexagonal group-III nitride alloys ($B_xM_{1-x}N$ with M = Al, Ga), predicts out-of-plane distortions in the stable structures of these materials. In addition to greater stability and larger band gaps, the puckered structure also leads to interesting polar ordering. Thus 2D boron-based hexagonal nitride alloys present a promising class of materials for the design of high-performance UWBG electronics with superior operating voltages, frequencies, and efficiencies, as well as intriguing electromechanical properties.

ACKNOWLEDGEMENT

The authors thank Tomas Palacios, Jing Kong, Jagadeesh Moodera and their research groups for valuable discussions. This work was supported mainly by Army Research Office Agreement Number W911NF-23-2-0057, and partly by ARO Agreement Number W911NF-21-1-0184 and ARO Cooperative Agreement Number W911NF-21-2-0147. Calculations were performed on the FASRC cluster supported by the FAS Division of Science Research Computing Group at Harvard University.

SUPPLEMENTARY INFORMATION

Technical details and parameters of first-principles calculations along with additional results of the structural and electronic properties of 2D nitride ordered alloys and related systems.

[1] J. Tsao, S. Chowdhury, M. Hollis, D. Jena, N. Johnson, K. Jones, R. Kaplar, S. Rajan, C. Van de Walle, E. Bellotti, *et al.*, Ultrawide-bandgap semiconductors: research opportunities and challenges, Adv. Electron. Mater. **4**, 1600501 (2018).
[2] W. Yang, K. Xin, J. Yang, Q. Xu, C. Shan, and Z. Wei, 2d ultrawide bandgap semiconductors: odyssey and challenges, Small Methods **6**, 2101348 (2022).
[3] M. H. Wong, O. Bierwagen, R. J. Kaplar, and H. Umezawa, Ultrawide-bandgap semiconductors: An overview, J. Mater. Res. **36**, 4601 (2021).
[4] K. S. Novoselov, A. K. Geim, S. V. Morozov, D.-e. Jiang, Y. Zhang, S. V. Dubonos, I. V. Grigorieva, and A. A. Firsov, Electric field effect in atomically thin carbon films, Science **306**, 666 (2004).
[5] M. Noor-A-Alam and M. Nolan, Engineering ferroelectricity and large piezoelectricity in h-bn, ACS Appl. Mater. Interfaces. **15**, 42737 (2023).
[6] A. Falin, Q. Cai, E. J. Santos, D. Scullion, D. Qian, R. Zhang, Z. Yang, S. Huang, K. Watanabe, T. Taniguchi, *et al.*, Mechanical properties of atomically thin boron nitride and the role of interlayer interactions, Nat. Commun. **8**, 15815 (2017).
[7] K. Watanabe, T. Taniguchi, and H. Kanda, Direct-bandgap properties and evidence for ultraviolet lasing of hexagonal boron nitride single crystal, Nat. Mater. **3**, 404 (2004).
[8] J. Ben, X. Liu, C. Wang, Y. Zhang, Z. Shi, Y. Jia, S. Zhang, H. Zhang, W. Yu, D. Li, *et al.*, 2d iii-nitride materials: Properties, growth, and applications, Adv. Mater. **33**, 2006761 (2021).
[9] K. Nam, J. Li, M. Nakarmi, J. Lin, and H. Jiang, Unique optical properties of algan alloys and related ultraviolet emitters, Appl. Phys. Lett. **84**, 5264 (2004).
[10] H. Jiang and J. Lin, Algan and inalgan alloys-epitaxial growth, optical and electrical properties, and applications, Opto-Electron. Rev. , 271 (2002).
[11] J.-X. Shen, D. Wickramaratne, and C. G. Van de Walle, Band bowing and the direct-to-indirect crossover in random baln alloys, Phys. Rev. Mater. **1**, 065001 (2017).
[12] S. Calderon, J. Hayden, S. M. Baksa, W. Tzou, S. Trolier-McKinstry, I. Dabo, J.-P. Maria, and E. C. Dickey, Atomic-scale polarization switching in wurtzite ferroelectrics, Science **380**, 1034 (2023).
[13] C. Milne, T. Biswas, and A. K. Singh, Ab initio prediction of ultra-wide band gap bxal1- xn materials, Adv. Electron. Mater. **9**, 2201197 (2023).
[14] C. L. Milne, T. Biswas, and A. K. Singh, Electronic properties of $b_xal_{1-x}n$ computed from gw simulations, arXiv:2309.16050 (2023).
[15] M. Zhang and X. Li, Structural and electronic properties of wurtzite $B_xAl_{1-x}N$ from first-principles calculations, Phys. Status Solidi B Basic Res. **254**, 1600749 (2017).
[16] Y. Chen, Y. Zhao, P. Ou, and J. Song, Two-dimensional iii-nitride alloys: electronic and chemical properties of monolayer $ga_{(1-x)}Al_xN$, Phys. Chem. Chem. Phys. **25**, 32549 (2023).
[17] F. Reis, G. Li, L. Dudy, M. Bauernfeind, S. Glass, W. Hanke, R. Thomale, J. Schäfer, and R. Claessen, Bismuthene on a sic substrate: A candidate for a high-

temperature quantum spin hall material, Science **357**, 287 (2017).
[18] R. Quhe, R. Fei, Q. Liu, J. Zheng, H. Li, C. Xu, Z. Ni, Y. Wang, D. Yu, Z. Gao, *et al.*, Tunable and sizable band gap in silicene by surface adsorption, Sci. Rep. **2**, 853 (2012).
[19] L. Tao, E. Cinquanta, D. Chiappe, C. Grazianetti, M. Fanciulli, M. Dubey, A. Molle, and D. Akinwande, Silicene field-effect transistors operating at room temperature, Nat. Nanotechnol. **10**, 227 (2015).
[20] C. Xu, G. Luo, Q. Liu, J. Zheng, Z. Zhang, S. Nagase, Z. Gao, and J. Lu, Giant magnetoresistance in silicene nanoribbons, Nanoscale **4**, 3111 (2012).
[21] F. Liu, C.-C. Liu, K. Wu, F. Yang, and Y. Yao, d+ i d chiral superconductivity in bilayer silicene, Phys. Rev. Lett. **111**, 066804 (2013).
[22] C.-C. Liu, W. Feng, and Y. Yao, Quantum spin hall effect in silicene and two-dimensional germanium, Phys. Rev. Lett. **107**, 076802 (2011).
[23] F. Xia, H. Wang, and Y. Jia, Rediscovering black phosphorus as an anisotropic layered material for optoelectronics and electronics, Nat. Commun. **5**, 4458 (2014).
[24] J. He, D. He, Y. Wang, Q. Cui, M. Z. Bellus, H.-Y. Chiu, and H. Zhao, Exceptional and anisotropic transport properties of photocarriers in black phosphorus, ACS Nano **9**, 6436 (2015).
[25] A.-L. Phaneuf-L'Heureux, A. Favron, J.-F. Germain, P. Lavoie, P. Desjardins, R. Leonelli, R. Martel, and S. Francoeur, Polarization-resolved raman study of bulk-like and davydov-induced vibrational modes of exfoliated black phosphorus, Nano Lett. **16**, 7761 (2016).
[26] L. Qi, S. Ruan, and Y.-J. Zeng, Review on recent developments in 2d ferroelectrics: Theories and applications, Adv. Mater. **33**, 2005098 (2021).
[27] H. Şahin, S. Cahangirov, M. Topsakal, E. Bekaroglu, E. Akturk, R. T. Senger, and S. Ciraci, Monolayer honeycomb structures of group-iv elements and iii-v binary compounds: First-principles calculations, Phys. Rev. B **80**, 155453 (2009).
[28] K. Yasuda, E. Zalys-Geller, X. Wang, D. Bennett, S. S. Cheema, K. Watanabe, T. Taniguchi, E. Kaxiras, P. Jarillo-Herrero, and R. Ashoori, Ultrafast high-endurance memory based on sliding ferroelectrics, Science , eadp3575 (2024).
[29] S. Lu, P. Shen, H. Zhang, G. Liu, B. Guo, Y. Cai, H. Chen, F. Xu, T. Zheng, F. Xu, *et al.*, Towards n-type conductivity in hexagonal boron nitride, Nature Communications **13**, 3109 (2022).
[30] S. Majety, T. C. Doan, J. Li, J. Lin, and H. Jiang, Electrical transport properties of si-doped hexagonal boron nitride epilayers, AIP Adv. **3** (2013).
[31] L. Weston, D. Wickramaratne, M. Mackoit, A. Alkauskas, and C. G. Van de Walle, Native point defects and impurities in hexagonal boron nitride, Phys. Rev. B **97**, 214104 (2018).
[32] Y. Yan and S.-H. Wei, Doping asymmetry in wide-bandgap semiconductors: Origins and solutions, physica status solidi (b) **245**, 641 (2008).
[33] D. Vanderbilt and R. King-Smith, Electric polarization as a bulk quantity and its relation to surface charge, Phys. Rev. B **48**, 4442 (1993).
[34] R. King-Smith and D. Vanderbilt, Theory of polarization of crystalline solids, Phys. Rev. B **47**, 1651 (1993).
[35] D. Bennett, W. J. Jankowski, G. Chaudhary, E. Kaxiras, and R.-J. Slager, Theory of polarization textures in crystal supercells, Phys. Rev. Res. **5**, 033216 (2023).
[36] P. Ghosez, J.-P. Michenaud, and X. Gonze, Dynamical atomic charges: The case of ABO_3 compounds, Phys. Rev. B **58**, 6224 (1998).
[37] D. Bennett and P. Ghosez, Asymmetric dynamical charges in two-dimensional ferroelectrics, arXiv:2404.10549 (2024).
[38] A. Chandrasekaran, A. Mishra, and A. K. Singh, Ferroelectricity, antiferroelectricity, and ultrathin 2d electron/hole gas in multifunctional monolayer mxene, Nano Lett. **17**, 3290 (2017).
[39] L. Meng, Y. Wang, L. Zhang, S. Du, R. Wu, L. Li, Y. Zhang, G. Li, H. Zhou, W. A. Hofer, *et al.*, Buckled silicene formation on ir (111), Nano letters **13**, 685 (2013).
[40] J.-H. Choi, P. Cui, W. Chen, J.-H. Cho, and Z. Zhang, Atomistic mechanisms of van der waals epitaxy and property optimization of layered materials, Wiley Interdisciplinary Reviews: Computational Molecular Science **7**, e1300 (2017).
[41] T. Aizawa, S. Suehara, and S. Otani, Silicene on zirconium carbide (111), The Journal of Physical Chemistry C **118**, 23049 (2014).
[42] C. D. Abernethy, G. M. Codd, M. D. Spicer, and M. K. Taylor, A highly stable N-heterocyclic carbene complex of trichloro-oxo-vanadium(v) displaying novel Cl—C(carbene) bonding interactions, J. Am. Chem. Soc. **125**, 1128 (2003).
[43] A. J. Arduengo, III, H. V. R. Dias, R. L. Harlow, and M. Kline, Electronic stabilization of nucleophilic carbenes, J. Am. Chem. Soc. **114**, 5530 (1992).
[44] A. J. Arduengo III, S. F. Gamper, J. C. Calabrese, and F. Davidson, Low-coordinate carbene complexes of nickel (0) and platinum (0), Journal of the American Chemical Society **116**, 4391 (1994).
[45] D. Wines, F. Ersan, and C. Ataca, Engineering the electronic, thermoelectric, and excitonic properties of two-dimensional group-iii nitrides through alloying for optoelectronic devices (b1–x al x n, al1–x ga x n, and ga1–x in x n), ACS Appl. Mater. Interfaces. **12**, 46416 (2020).
[46] T. Akiyama, K. Nakamura, and T. Ito, Effects of lattice constraint on structures and electronic properties of baln and bgan alloys: A first-principles study, Applied Physics Express **11**, 025501 (2018).
[47] C. Kim, G. Pilania, and R. Ramprasad, Machine learning assisted predictions of intrinsic dielectric breakdown strength of abx3 perovskites, The Journal of Physical Chemistry C **120**, 14575 (2016).
[48] C. R. Dean, A. F. Young, I. Meric, C. Lee, L. Wang, S. Sorgenfrei, K. Watanabe, T. Taniguchi, P. Kim, K. L. Shepard, *et al.*, Boron nitride substrates for high-quality graphene electronics, Nat. Nanotechnol. **5**, 722 (2010).
[49] J. Xue, J. Sanchez-Yamagishi, D. Bulmash, P. Jacquod, A. Deshpande, K. Watanabe, T. Taniguchi, P. Jarillo-Herrero, and B. J. LeRoy, Scanning tunnelling microscopy and spectroscopy of ultra-flat graphene on hexagonal boron nitride, Nat. Mater. **10**, 282 (2011).
[50] J. Lyons, A. Janotti, and C. Van de Walle, Effects of hole localization on limiting p-type conductivity in oxide and nitride semiconductors, J. Appl. Phys. **115** (2014).
[51] L. Weston, D. Wickramaratne, and C. Van de Walle, Hole polarons and p-type doping in boron nitride polymorphs,

Physical Review B **96**, 100102 (2017).
[52] H. Şahin, S. Cahangirov, M. Topsakal, E. Bekaroglu, E. Akturk, R. T. Senger, and S. Ciraci, Monolayer honeycomb structures of group-iv elements and iii-v binary compounds: First-principles calculations, Phys. Rev. B **80**, 155453 (2009).
[53] H. Jónsson, G. Mills, and K. W. Jacobsen, Nudged elastic band method for finding minimum energy paths of transitions, in *Classical and quantum dynamics in condensed phase simulations* (World Scientific, 1998) pp. 385–404.
[54] Supplemental Material, See Supplemental Material at URL provided by the publisher for technical details and parameters of first-principles calculations along with additional results of the structural and electronic properties of two-dimensional nitride ordered alloys and related systems. The Supplemental Material also contains Refs. [55-61].
[55] P. Giannozzi, S. Baroni, N. Bonini, M. Calandra, R. Car, C. Cavazzoni, D. Ceresoli, G. L. Chiarotti, M. Cococcioni, I. Dabo, *et al.*, Quantum espresso: a modular and open-source software project for quantum simulations of materials, Journal of physics: Condensed matter **21**, 395502 (2009).
[56] J. P. Perdew, K. Burke, and M. Ernzerhof, Generalized gradient approximation made simple, Physical review letters **77**, 3865 (1996).
[57] J. Furthmüller, J. Hafner, and G. Kresse, Dimer reconstruction and electronic surface states on clean and hydrogenated diamond (100) surfaces, Physical Review B **53**, 7334 (1996).
[58] G. Kresse and J. Furthmüller, Efficiency of ab-initio total energy calculations for metals and semiconductors using a plane-wave basis set, Computational materials science **6**, 15 (1996).
[59] P. E. Blöchl, Projector augmented-wave method, Physical review B **50**, 17953 (1994).
[60] S. Baroni, S. De Gironcoli, A. Dal Corso, and P. Giannozzi, Phonons and related crystal properties from density-functional perturbation theory, Reviews of modern Physics **73**, 515 (2001).
[61] X. Hua, X. Chen, and W. Goddard, Generalized generalized gradient approximation: An improved density-functional theory for accurate orbital eigenvalues, Physical Review B **55**, 16103 (1997).